Spreading and sedimentation from bottom-propagating particle-bearing jets

Mohnish Kapil[1], **Bruce R. Sutherland**[2,3],† **and Sridhar Balasubramanian**[1,4],†

[1]Department of Mechanical Engineering, Indian Institute of Technology Bombay, Mumbai, MH 400076, India

[2]Department of Physics, University of Alberta, Edmonton, AB T6G 2E1, Canada

[3]Department of Earth and Atmospheric Sciences, University of Alberta, Edmonton, AB T6G 2E3, Canada

[4]IDP in Climate Studies, Indian Institute of Technology Bombay, Mumbai, MH 400076, India

Laboratory experiments are conducted to examine the evolution of and sedimentation from a particle-bearing jet advancing along a horizontal or downward-sloping boundary underlying a uniform-density ambient fluid. The jet front advances along the bottom while exhibiting a self-similar profile. As the jet propagates downstream, particles settle out, resulting in a teardrop-shaped sediment bed whose geometric parameters are measured non-intrusively using a light attenuation technique. The bed shape is well represented by the theory that assumes a Gaussian radial profile of velocity within the jet and accounts for the bedload transport of particles after they settle. In particular, the bed length is given by $l_0 = (1.8 \pm 0.4)[M_0/(g'd_p)]^{1/2}$, in which M_0 is the source momentum flux, g' is the reduced gravity of the particles and d_p is the particle diameter. The corresponding scale for the sediment depth captures the anticipated order of magnitude for the maximum depth of deposit, but the measurements indicate additional dependence upon M_0, suggesting that the morphology of the bed non-negligibly influences particle settling.

Key words: jets, sediment transport, particle/fluid flow

1. Introduction

Particles are carried along a bottom boundary by jets in many naturally occurring systems and industrial processes. If the particle density and volume concentration are sufficiently large, the jets are said to be particle-laden, meaning that the particles have a non-negligible influence upon the buoyancy of the jet relative to the ambient fluid. An extreme example of a particle-laden flow is a turbidity current, which is driven primarily by buoyancy forces associated with the density of the particle–fluid mixture in comparison with the lower-density ambient fluid (Bonnecaze, Huppert & Lister 1993; Bonnecaze & Lister 1999; Kneller & Buckee 2000; Meiburg & Kneller 2010). Turbidity currents ultimately stop when the particles have rained out and the buoyancy driving force is exhausted. Conversely, in a particle-bearing jet the particle concentration is so small that the particles have a negligible influence upon buoyancy. Although particles

† Email addresses for correspondence: bruce.sutherland@ualberta.ca, sridharb@iitb.ac.in

rain out of the jet to sediment on the bottom, the jet continues to advance and this can additionally influence the sediment morphology through bedload transport (Gomez 1991). A common motivation for studying particle-bearing or particle-laden jets is to understand the sedimentary deposits that build up as particles rain out of the jet, whether oriented vertically (Shuen *et al.* 1985; Fleckhaus, Hishida & Maeda 1987; Hardalupas *et al.* 1989; Sutherland & Hong 2016; Balasubramanian, Mirajkar & Banerjee 2018) or horizontally. In the latter case, this has been studied non-intrusively for turbidity currents by measuring resistivity between floor-mounted electrodes (de Rooij & Dalziel 2001). In our present study, we use the method of light attenuation adapted to particle deposits (Munro & Dalziel 2005) in order to measure the structure of sediments from a particle-bearing jet. We furthermore adapt the methodology recently devised by Bhamidipati & Woods (2017), who examined the structure of vertically rising plumes to study the frontal structure and interior motion of the plume in a stratified ambient.

The presence of particles in turbulent jets and gravity currents is known to alter the flow dynamics significantly depending upon their concentration, density and diameter (Picano *et al.* 2011; Lee, Li & Lee 2013; Lippert & Woods 2020; Sutherland, Rosevear & Cenedese 2020). Even at low concentrations (with particle volume fractions less than 1 %), the dynamics for particle settling within a turbulent jet is known to be quite complex. In particular, Lee *et al.* (2013) used laboratory experiments to examine the settling of particles from a horizontal jet situated well above the tank bottom. Within half the momentum-settling length scale, the particle distribution in the jet was found to be approximately axisymmetric around the jet centreline. Beyond this distance the particle settling from the underside of the jet resulted in a horseshoe-shaped pattern of particle concentration contours. Likewise, the numerical study of a particle-bearing jet by Picano *et al.* (2011) showed an enhanced concentration of particles near the jet axis, being largest when the local Stokes number (the ratio of the particle relaxation time to the integral time scale of the turbulent flow) was near unity. A recent study by Lippert & Woods (2020) examined particle settling in a gravity current driven by the buoyancy of the particles. They showed that the mixing near the top interface of the current governed the development of a particle-settling front provided the speed of the current was sufficiently large, but not too large, compared with the setting velocity.

Although there have been many investigations into sedimentation from turbidity currents and other manifestations of particle-laden currents, there are few studies of sedimentation from particle-bearing gravity currents and jets. In a recent study, Sutherland *et al.* (2020) examined sedimentation resulting from particles descending from a buoyant current running under an upper slope – a model for sediment transport by subglacial meltwater plumes. They showed that particles descending from below the current were carried towards the current source as a consequence of an underlying return flow set up by entrainment into the overlying current. The resulting deposition pattern had a near-uniform slope with the depth decreasing with distance from the source. In that study, the return flow was relatively slow so that the settled particles were unaffected by the overlying flow. In contrast, bottom-propagating gravity currents and jets may continue to act upon the particle motion due to bedload transport even after they have settled.

In the study of sediment transport by statistically steady turbulent river flows, bedload transport and resuspension are typically characterized by a Shields parameter (Shields 1936), which measures the bottom stress relative to the weight per area of the particles. If the particles are sufficiently small, the turbulent shear stresses may not be able to overcome the viscous stresses exerted on the particles in the bottom boundary layer. While examining particle resuspension by an impacting rigid body, Eames & Dalziel (2000) showed that the

critical Shields parameter for mobilization of tiny particles was inversely proportional to the square root of the particle Reynolds number.

In the many studies of bedload transport by river flows and wind flows over deserts, a focus has been on the bedforms that naturally develop into dunes (Hersen, Douady & Andreotti 2002; Charru, Andreotti & Claudin 2013; Bacik *et al.* 2020). In most of these examinations, the overlying turbulent flow was statistically horizontally uniform. In part motivating our work is the study of bedforms that develop from a jet emanating from a localized source such that the turbulence characteristics decay laterally as well as in the along-jet direction.

In § 2, a review of the relevant theory for turbulent jets and sediment bedload transport is presented. In § 3, the experimental set-up and the method employed for data analysis are described. The quantitative results are presented in § 4 and conclusions are given in § 5.

2. Theoretical considerations

Here we review the classical theory for unbounded statistically steady, neutrally buoyant, self-similar turbulent jets and adapt it for a wall jet. We further use the approach of Bhamidipati & Woods (2017) to develop a semi-empirical prediction for the advance of the jet front. We go on to develop a theory for the pattern of sediment deposition arising from a particle-bearing jet flowing along a rigid boundary, adapting this to account for bedload transport of particles after they have rained out of the jet.

2.1. *Self-similar jet theory*

Because our focus is primarily on horizontally oriented jets, we characterize the steady along-jet flow by $u(r, x)$, in which x is the distance from the source in the along-jet direction and r is the radial distance from the centreline of the jet. For the later purposes of examining particle deposition from the jet, we assume the mean flow varies radially as a Gaussian according to

$$u(r, x) = u_c(x) \exp\left(-\frac{r^2}{b(x)^2}\right), \tag{2.1}$$

in which $b(x)$ is a measure of the jet width and $u_c(x)$ is the centreline velocity. In our study of a wall jet, it is assumed that the flow is of sufficiently high Reynolds number that the viscous boundary layer between the wall and jet is negligibly small compared with the jet width. This allows us to use (2.1) to characterize the mean flow in the upper half $y-z$ plane, with y being the horizontal spanwise distance from the jet centreline and z being the normal distance from the tank bottom. It may be that, due to the influence of the wall, the actual cross-section of the jet is semi-elliptical instead of circular, as postulated by McConnochie, Cenedese & McElwaine (2020) in their study of a wall fountain. In this case b^2 would be related to the product of the lateral and vertical extent of the jet. Nonetheless, if it is assumed that the aspect ratio is fixed with downstream distance x, then the form given by (2.1) suffices for the analyses that follow.

The jet dynamics is governed primarily by the momentum flux, M_0, and volume flux, Q_0, at the source. For fluid emanating from a nozzle of radius b_0 with mean speed u_0, $Q_0 = \pi b_0^2 u_0$ and $M_0 = \pi b_0^2 u_0^2$. Shortly after exiting the nozzle near the tank bottom the flow is taken to adopt the mean flow structure given by (2.1). The transition distance and

time are naturally defined by the jet length and time scales given, respectively, by

$$L_Q = \frac{Q_0}{M_0^{1/2}} \quad \text{and} \quad T_Q = \frac{Q_0^2}{M_0^{3/2}}. \quad (2.2a,b)$$

The former scale provides a measure of the distance from the actual source to the virtual origin; the latter measures the time to traverse this distance (Hunt & Kaye 2005).

The equations for a statistically steady turbulent jet in a uniform ambient fluid (Morton, Taylor & Turner 1956) are given in the upper half plane by

$$\frac{dQ}{dx} = \pi \alpha_g b u_c, \quad (2.3)$$

in which

$$Q \equiv \frac{\pi}{2} b^2 u_c \quad (2.4)$$

is the volume flux for the wall jet and α_g is the entrainment coefficient for a Gaussian jet, representing the assumption that the lateral inflow velocity is proportional to the centreline velocity. In experiments of unbounded jets, typical values of the entrainment coefficient are found to lie in the range $0.046 < \alpha_g < 0.059$ (Carazzo, Kaminski & Tait 2006). In contrast, the entrainment coefficient for plumes is larger, with $0.071 < \alpha_{gp} < 0.11$ (Morton 1959; Carazzo *et al.* 2006; van Reeuwijk *et al.* 2016; Parker *et al.* 2020). As is well known for plumes, the presence of a vertical wall along the plume centreline reduces entrainment, with a recent study showing a reduction from $\alpha_{gp} \simeq 0.10$ for a free plume to $\alpha_{gp} \simeq 0.061$ for a wall plume (Parker *et al.* 2020). Likewise, a corresponding reduction in the entrainment coefficient of a wall jet is anticipated. The effect of buoyancy in momentum-driven regions is characterized by the jet length scale L_m, defined by

$$L_m = \frac{M_0^{3/4}}{B_0^{1/2}}, \quad (2.5)$$

in which

$$B_0 = (g'Q_0)\phi_v \quad (2.6)$$

is the buoyancy flux at the source, $g' = (\rho_p - \rho)g/\rho$ is the reduced gravity, with ρ_p being the particle density and ρ the fluid density, and ϕ_v is the volume fraction of particles in the fluid. At distances from the source beyond L_m, the flow would be governed significantly by buoyancy. However, for our case of a particle-bearing jet with $\phi_v < 1\%$, the source buoyancy is so small that the particles settle out at much shorter distances than L_m. And, of course, as the particles rain out the influence of their buoyancy in the jet becomes further reduced. For this reason, buoyancy effects are neglected. Hence momentum is conserved in the jet such that the momentum flux in the upper half plane

$$M = M_0 \equiv \frac{1}{4}\pi b^2 u_c^2 \quad (2.7)$$

is constant. Using this to replace b with $2(M_0/\pi)^{1/2}/u_c$ in (2.3) and (2.4), and then integrating gives an expression for the centreline velocity, u_c, as it depends upon distance,

x, from the point source (virtual) origin:

$$u_c(x) = \xi_0 \frac{M_0^{1/2}}{x}. \tag{2.8}$$

In (2.8), the non-dimensional constant

$$\xi_0 \equiv \frac{1}{\sqrt{\pi}\,\alpha_g} \tag{2.9}$$

is an empirical parameter replacing the role of α_g. The corresponding jet radius is predicted to increase linearly with distance from the virtual origin as

$$b(x) = \frac{2}{\sqrt{\pi}\xi_0}x. \tag{2.10}$$

While (2.8) gives the flow within a statistically steady turbulent jet, it is expected that the advance of the front of a starting jet should have the same dimensional dependence upon $M_0^{1/2}/x$. Because the jet is injected continuously, the front is not influenced by strong vortex ring formation and it is considered to be quasi-steady after undergoing initial adjustments (Gharib, Rambod & Shariff 1998). Following the approach of Bhamidipati & Woods (2017) in their study of vertically rising starting plumes, we assume the front position $x_f(t)$ satisfies $\mathrm{d}x_f/\mathrm{d}t = \xi_f M_0^{1/2}/x_f$, in which ξ_f is a non-dimensional measure of the front velocity. Integrating and rearranging gives an expression for ξ_f:

$$\xi_f = \frac{x_f^2}{2M_0^{1/2}(t+t_0)}, \tag{2.11}$$

in which t_0 represents the time required for the jet to attain a self-similar shape (Bhamidipati & Woods 2017). We will show that, with the correct choice of t_0, ξ_f is indeed nearly constant for sufficiently large t irrespective of the flow and particle parameters. However, the scaling described above will not be appropriate at large distances when the vertical extent of the jet becomes a significant fraction of the total fluid depth, in which case the flow of the ambient fluid over and around the jet becomes non-negligible. In our experiments, the vertical extent of the jet is $\simeq 3/4$ the total depth after propagating a distance from the source of $x \approx 40$ cm and $x \approx 60$ cm, respectively, for bottom slope angles of $0°$ and $8°$. Most of our analyses of jet spreading and sediment deposition are well within this range of x.

2.2. *Sedimentation*

To derive a simple model for predicting the onset of sedimentation from a particle-bearing jet, we suppose that the particles are homogeneously spread within the vertical cross-section of the jet and they begin to settle out when the Gaussian profile of the jet speed near the bottom becomes comparable to the particle settling velocity, w_p. Setting $w_p = u(r_p, x)$ in (2.1) thus gives an implicit formula for the critical radius $r_p(x)$ which is defined as the distance from $y = 0$ in the horizontal plane at which particles settle.

Explicitly,

$$r_p(x) = \frac{2}{\sqrt{\pi}} \frac{x}{\xi_0} \left[\ln \left(\xi_0 \frac{L_p}{x} \right) \right]^{1/2}, \tag{2.12}$$

in which we have used (2.8) and (2.10) along with the momentum-settling length scale L_p, which is defined to be (Ernst *et al.* 1996)

$$L_p \equiv \frac{M_0^{1/2}}{w_p}. \tag{2.13}$$

In (2.12), x is bounded above by $\xi_0 L_p$, representing the maximum distance from the virtual origin beyond which particle settling must occur.

While (2.12) may be representative of where particles first descend to the bottom, it is possible for the particles consequently to slide along the bottom as a consequence of stresses imposed by the overlying flow through a process known as bedload transport. Whether the stresses are sufficiently strong to advect the settled particles is determined by the Shields parameter (Shields 1936), defined as

$$Sh = \frac{u^2}{g' d_p}, \tag{2.14}$$

in which u is the local flow velocity far from the boundary, d_p is the particle diameter and $g' = (\rho_p - \rho)g/\rho$ is the reduced gravity. Bedload transport occurs if u is sufficiently large that Sh exceeds a critical value, Sh_c, of order unity. The critical velocity below which no bedload transport occurs is thus given by $(Sh_c g' d_p)^{1/2}$. Equating this with (2.1) and rearranging, as in (2.12), the prediction for the interior boundary of the sediment bed is given by

$$r_s(x) = \frac{2}{\sqrt{\pi}} \frac{x}{\xi_0} \left[\ln \left(\xi_0 \frac{\gamma_s L_s}{x} \right) \right]^{1/2}, \tag{2.15}$$

in which

$$L_s \equiv \left(\frac{M_0}{g' d_p} \right)^{1/2}. \tag{2.16}$$

For convenience, we have defined $\gamma_s \equiv Sh_c^{-1/2}$, which is an empirical quantity to be determined from experiments.

In the above discussion, it was assumed the particles were much larger than the viscous boundary layer associated with the ambient flow passing over the bottom wall. If the particles are much smaller than the boundary layer depth, $\delta \sim \nu/u$, in which ν is the kinematic viscosity, then the velocity of the flow acting on the particles is of order $u_\nu \sim d_p u/\delta = Re_f u$, in which

$$Re_f \equiv \frac{u d_p}{\nu} \tag{2.17}$$

is the Reynolds number based upon the local ambient flow speed. Consequently, the condition for bedload transport, given by $u_\nu \sim (g' d_p)^{1/2}$, can be recast in terms of u. Putting this expression in (2.14) gives the critical condition for bedload transport to be

$Sh_c \sim Re_p^{-1/2}$ (Eames & Dalziel 2000), in which

$$Re_p \equiv \frac{w_p d_p}{\nu} \tag{2.18}$$

is the particle Reynolds number. Recasting this critical condition in terms of the critical ambient flow speed, u_s, outside the boundary layer gives

$$u_s = \frac{1}{\gamma_c} (g' d_p)^{1/2} Re_p^{-1/4}, \tag{2.19}$$

in which γ_c is a non-dimensional empirical constant to be determined empirically. The location where particles ultimately sediment is therefore predicted to occur where $u_s = u(r, x)$. Rearranging, as in (2.12), we predict the sediment bed should begin to accumulate beyond a radius

$$r_c(x) = \sqrt{\frac{2}{\pi} \frac{x}{\xi_0}} \left[\ln \left(\xi_0 \frac{\gamma_c L_c}{x} \right) \right]^{1/2}, \tag{2.20}$$

in which

$$L_c \equiv \frac{M_0^{1/2}}{u_s}. \tag{2.21}$$

If $Re_p \ll 1$, w_p is given by the Stokes settling formula, in which case $L_c = [(M_0^2 d_p)/(18 g' \nu^2)]^{1/4}$. For our experiments, in which Re_p ranges between 0.5 and 8, we use the empirical formulae equations (24), (25) and (37) of Brown & Lawler (2003), which account for the correction to the Stokes settling velocity due to particle inertia at these moderate particle Reynolds numbers.

The above equations, (2.12), (2.15) and (2.20), defining the inner boundary of the sediment bed will be compared below with experiment results to determine, respectively, if bedload transport is not important or, if it is important, whether the boundary layer has negligible influence on bedload transport ($Re_f \gg 1$) or if it is significant ($Re_f \ll 1$).

3. Experimental set-up and analysis methods

Here we describe the apparatus used for performing the experiments along with the techniques used for data analysis. A schematic of the experimental set-up is shown in figure 1.

3.1. *Apparatus*

The experiments were performed in a tank with length $L_T = 120$ cm, width $W_T = 120$ cm and height $H_T = 30$ cm. This was suspended above the floor by four supports at the corners. In some experiments, the two supports were higher at the rear of the tank such that it sloped downward at a prescribed angle $\beta = 8°$ to the horizontal. A nozzle with diameter $d = 1$ cm was positioned at the mid-span of the tank with its opening parallel to the bottom, situated 35 cm from the rear end of the tank. The nozzle consisted of an expansion chamber that led to a fine mesh covering a 0.2 cm radius opening. This set-up ensured turbulent flow exited the nozzle (Hunt & Linden 2001). Leading to the nozzle was 1 cm inner diameter flexible Tygon tubing connected to a hopper-shaped reservoir. This was a cylinder of height $H_R = 50$ cm and radius $R = 15$ cm which had a conical bottom sloping at an angle of 30° to an opening at the bottom. Two angled mixers were situated
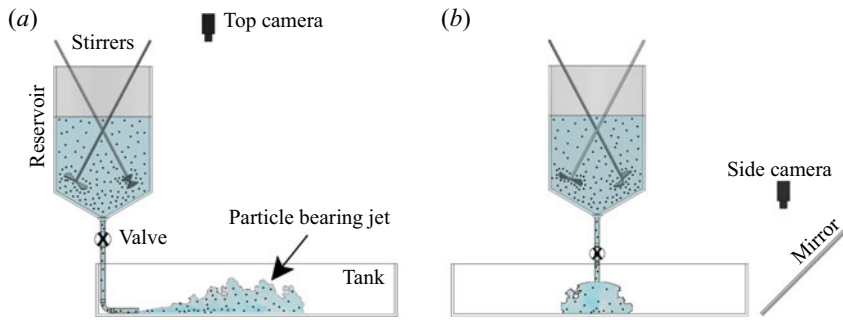
FIGURE 1. Schematic of the experimental set-up showing (*a*) the side view and (*b*) the front view with the jet approaching the viewer.

inside the reservoir to ensure sufficient turbulent motion to keep particles in uniform suspension before and during an experiment. The hose itself passed through a valve, which was opened at the start of an experiment, and a clamp which was used to adjust the source volume flux, Q_0, leaving the nozzle. Tap water was put into both the tank and reservoir such that the maximum depth of water in the tank was 15 cm and the depth of water in the reservoir was 25 cm. With the base of the reservoir being situated 100 cm above the location of the nozzle, the flow was driven by near-constant pressure: during the course of an experiment, the depth of fluid in the reservoir decreased by no more than 1 cm for a total change in distance between the reservoir surface and nozzle of less than 1 %.

Shortly before the start of an experiment, the mixers in the reservoir were turned on, and 10 ml of blue food colouring was added. Then a pre-measured mass of glass ballotini, having density $\rho_p = 2.5$ g cm^{-3}, was added to the reservoir. Depending upon the experiment, the spheres had mean diameters of $d_p \approx 88 \pm 10$, 120 ± 30 or 212 ± 40 μm. From the mass and size of the spheres and the known volume of fluid initially in the reservoir, the volume fraction of particles in the fluid, ϕ_v, was determined. To ensure that the particles had negligible influence upon buoyancy in the jet, all experiments had $\phi_v \leqslant 0.01$. The typical Reynolds number of the jet at the source ranged from 4500 to 9000 in all the experiments.

A list of all the experiments performed with corresponding parameters presented in this study is given in table 1. Several runs were repeated two to three times as a check of the consistency of results.

At the start of an experiment, the valve was opened resulting in the release of a particle-bearing jet in the tank. When the jet front reached the front of the tank, the valve was closed, and the experiment ended. The average run time of the experiments lasted from 10 to 40 s depending upon Q_0. In some experiments, red dye was impulsively injected into the tubing connecting the reservoir to the nozzle. This was done in order to distinguish the flow within the jet from the velocity at its front.

In order to visualize and record top views of the experiments, a light-emitting diode panel was situated underneath the tank and a digital camera (Canon Rebel T3i) situated 185 cm above the centre of the tank was directed vertically downward. Simultaneously, a second camera (Canon Rebel T5i) was positioned to look downward 50 cm above an angled mirror to give a side view of the experiment. Both cameras captured images at a rate of 24 frames per second with a resolution of ≈ 11 px cm^{-1}.

Images from a typical experiment are shown in figure 2. The side views show that the jet emanating from the nozzle touches the tank bottom shortly after exiting the nozzle.

Exp.	ϕ_v	d_p (μm)	Q_0 (cm^3 s^{-1})	M_0 (cm^4 s^{-2})	β (deg.)	L_Q (cm)	T_Q (s)
1	0	0	48	3233	8	0.84	0.0125
2	0.001	120	48	3233	8	0.84	0.0125
3	0.002	120	48	3233	8	0.84	0.0125
4	0.003	120	48	3233	8	0.84	0.0125
5	0.004	120	48	3233	8	0.84	0.0125
6	0.005	120	48	3233	8	0.84	0.0125
7	0.01	120	48	3233	8	0.84	0.0125
8	0.002	88	48	3233	8	0.84	0.0125
9	0.005	88	48	3233	8	0.84	0.0125
10	0.002	220	48	3233	8	0.84	0.0125
11	0.005	220	48	3233	8	0.84	0.0125
12	0.01	220	48	3233	8	0.84	0.0125
13	0	0	30	1263	8	0.84	0.02
14	0.002	120	30	1263	8	0.84	0.02
15	0.005	120	30	1263	8	0.84	0.02
16	0.01	120	30	1263	8	0.84	0.02
17	0	0	60	5052	8	0.84	0.01
18	0.002	120	60	5052	8	0.84	0.01
19	0.005	120	60	5052	8	0.84	0.01
20	0.01	120	60	5052	8	0.84	0.01
21	0	0	48	3233	0	0.84	0.0125
22	0.001	120	48	3233	0	0.84	0.0125
23	0.002	120	48	3233	0	0.84	0.0125
24	0.003	120	48	3233	0	0.84	0.0125
25	0.004	120	48	3233	0	0.84	0.0125
26	0.005	120	48	3233	0	0.84	0.0125
27	0.01	120	48	3233	0	0.84	0.0125
28	0.002	88	48	3233	0	0.84	0.0125
29	0.005	88	48	3233	0	0.84	0.0125
30	0.002	220	48	3233	0	0.84	0.0125
31	0.005	220	48	3233	0	0.84	0.0125
32	0.01	220	48	3233	0	0.84	0.0125
33	0.002	120	30	1263	0	0.84	0.02
34	0.005	120	30	1263	0	0.84	0.02
35	0.01	120	30	1263	0	0.84	0.02
36	0.002	88	30	1263	0	0.84	0.02
37	0.005	88	30	1263	0	0.84	0.02
38	0.002	220	30	1263	0	0.84	0.02
39	0.005	220	30	1263	0	0.84	0.02
40	0.01	220	30	1263	0	0.84	0.02
41	0.002	120	60	5052	0	0.84	0.01
42	0.005	120	60	5052	0	0.84	0.01
43	0.01	120	60	5052	0	0.84	0.01

TABLE 1. Source parameters for all the experiments: experiment number (Exp.), particle volume fraction (ϕ_v), particle diameter (d_p), volume flux (Q_0), momentum flux (M_0) and corresponding calculated jet length scale, L_Q, and time scale, T_Q.

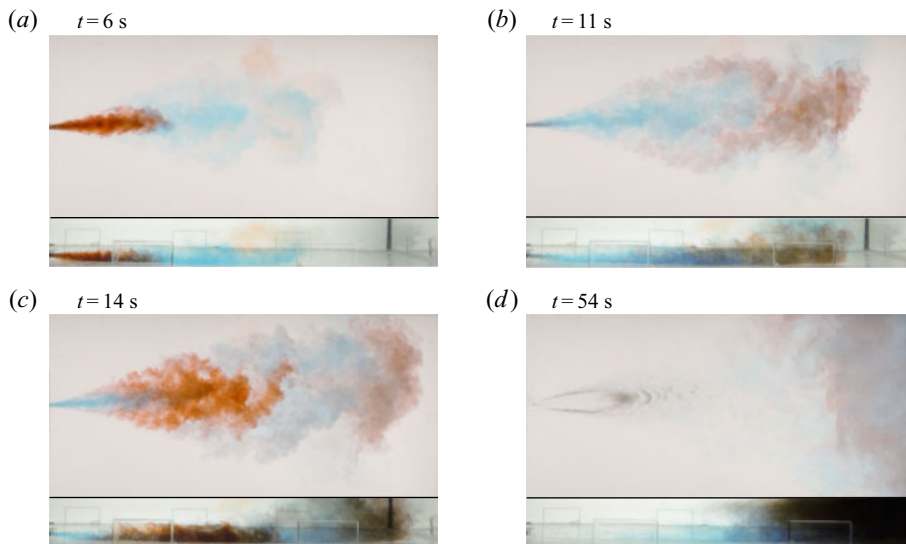FIGURE 2. Top-view (upper image of each panel) and side-view (lower image of each panel) snapshots of Experiment 23 with $Q_0 = 48$ cm^3 s^{-1}, $\phi_v = 0.002$, $d_p = 120$ µm and $\beta = 0°$ shown at (*a*–*d*) four times as indicated. Red dye is impulsively injected into the hose leading to the nozzle shortly before 6 and 14 s. The image at 54 s shows the teardrop-shaped sediment deposit near the nozzle 10 s after the valve is closed. Snapshot dimensions: length $= 83$ cm, width $= 40$ cm (top view) and height $= 10$ cm (side view).

The top of the jet lies well below the free surface up to 80 cm from the nozzle. This is relevant because most sediments are deposited well before this distance indicating that the finite depth has little influence upon the deposition process, although we will show that it does influence entrainment into the jet far downstream of the source.

For the experiment shown in figure 2, red dye was impulsively injected into the hose near the nozzle at two times after the experiment began. This clearly showed that fluid from the rear continuously reached the front of the blue-dyed jet before being swept sideways. A similar observation was made by Bhamidipati & Woods (2017) in their examination of vertically rising plumes. This effect could be attributed to the additional drag exerted on the front of the jet as it impinges upon a quiescent ambient fluid.

3.2. *Analysis of jet*

Digital movies from the top view of the experiments were processed using MatLab. To determine the position and shape of the blue-dyed jet front, for each frame of the recordings the image of the background in the absence of a jet was subtracted. The front and sides of the jet were then tracked by thresholding the image intensity to 20 % of the maximum intensity value. In order to quantify the error in measurement of the front location, $x_f(t)$, different thresholding values were used, giving a location accuracy to within ± 5 %.

3.3. *Light attenuation technique*

Figure 2(*d*) shows a typical sediment pattern that formed after the end of an experiment. The teardrop shape of the sediment bed was observed for all the experiments.
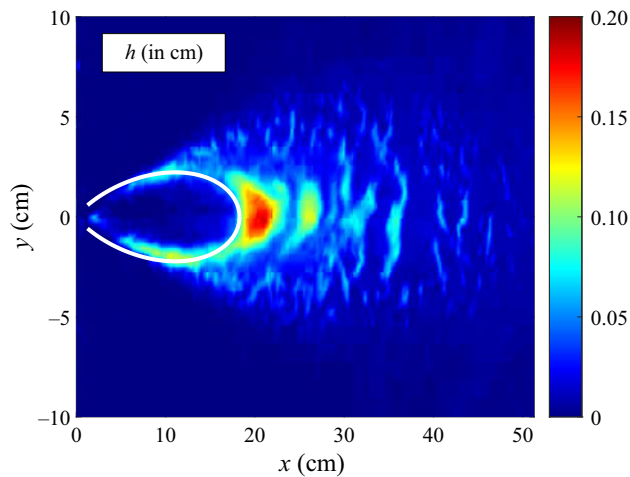
FIGURE 3. Depth of the sediment deposit computed at the end of Experiment 6, which has $\phi_v = 0.5\,\%$ and $d_p = 120\ \mu$m. The superimposed curve shows the predicted onset of sediment deposition according to (2.15), which includes the effect of bedload transport for $Re_f \gg 1$.

The sediment depth was measured non-intrusively using the method of light attenuation (Munro & Dalziel 2005; Sutherland & Hong 2016). Because the particles were composed of glass spheres, light was scattered but not obstructed by the particles. Consequently, the light passing through the sediment is expected to decrease exponentially with the sediment depth, h. Explicitly, the light intensity, I, is expected to depend upon h as

$$I = I_b + (I_0 - I_b)\,\mathrm{e}^{-h/\sigma_h}. \tag{3.1}$$

This involves three empirically determined parameters: I_b is the effective 'black' intensity corresponding to a sediment depth so large that light no longer passes through it; I_0 is the intensity in the absence of particles; and σ_h is the e-folding depth over which the intensity difference decreases by a factor e. The parameters were determined using a straight-edged scraper to make a linearly decreasing slope over a distance of 20 cm between a 1 cm tall guide and the bottom of a 'calibration tank'. By recording the intensity of light passing through this uniform slope, a measurement of $I(h)$ was found. A nonlinear regression routine in MatLab was then used to determine a best-fit curve of the form (3.1). This procedure was followed for each of the three particle types. (See, for example, Sutherland & Hong (2016) for details of the calibration procedure.)

Once I_b, I_0 and σ_h were determined, it was straightforward to invert (3.1) to determine h for given I. As an example, figure 3 shows the measured sediment depth corresponding to Experiment 6.

4. Quantitative results

4.1. *Bulk dynamics*

Figure 4(*a*) shows the outline of the jet at successive times as it advances and spreads laterally. Normalizing both the along-jet distance, x, and radial distance, r, with the front position, x_f, leads to an approximately self-similar profile (figure 4*b*). These scaled profiles are then averaged to produce plots of the mean relative spread of the current with relative distance from the source. Figure 4(*c*) plots these mean profiles computed for experiments
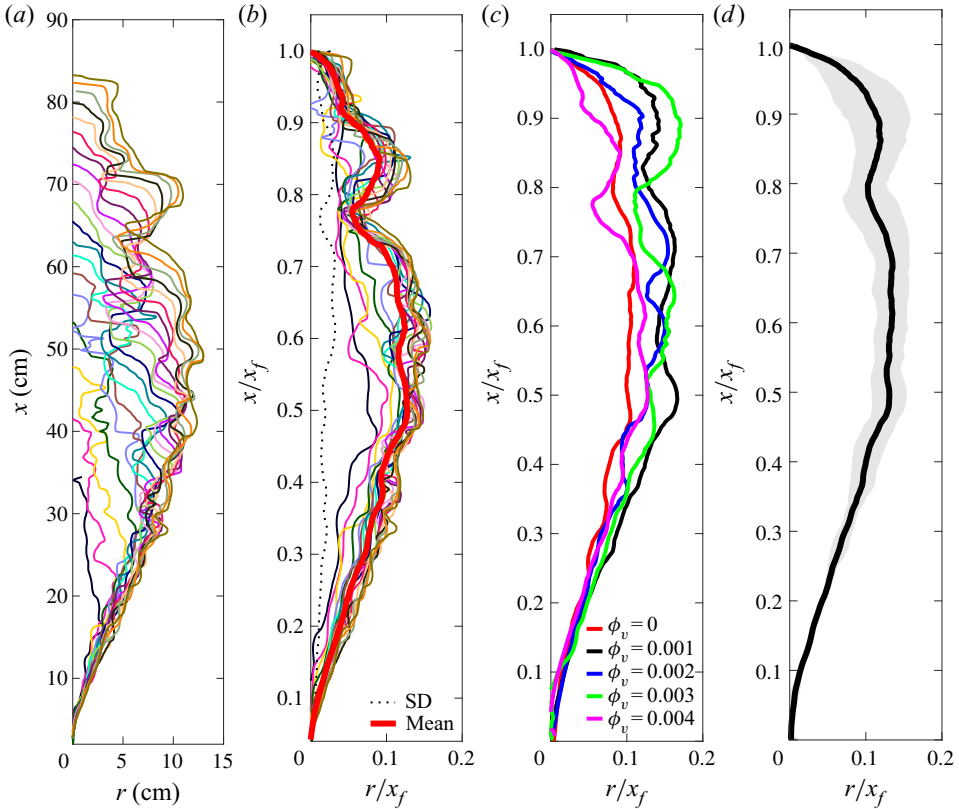
FIGURE 4. From Experiment 5, (*a*) lateral extent of the jet as a function of along-jet coordinate *x* plotted at time steps $= 0.5$ s starting from $t = 2$ s, (*b*) corresponding lateral extent with along-jet coordinate scaled by the front position x_f, (*c*) average (solid lines) of the scaled front positions from Experiments 1, 2, 3, 4 and 5 with different particle concentrations ϕ_v, having fixed $Q_0 = 48$ cm^3 s^{-1}, $d_p = 120$ µm and $\beta = 8°$ and (*d*) mean profile (line) and standard deviation (grey shaded region) computed from Experiments 1, 2, 3, 4 and 5.

of jets with different particle concentrations, ϕ_v. As expected for particle-bearing (not particle-laden) jets, the profiles effectively overlap, indicating that the particles have negligible influence upon the jet evolution. Taking the radial mean of all these profiles for each *x* gives the self-similar jet profile plotted in figure 4(*d*). The standard deviation about the mean becomes large only near the front of the jet where greater fluctuations occur as a consequence of the impinging head interacting with the ambient fluid and due to recirculation patterns occurring in the lee of the head, where the fluid in the jet catches up to the front and then spreads laterally, as shown in figure 2.

As well as having a self-similar shape, the advance of the jet front is self-similar in time. This is shown in figure 5, which plots the front position of the jet in time from experiments with different values of Q_0. Upon non-dimensionalizing position and time, respectively, with the characteristic scales L_Q and T_Q, the curves collapse well, as shown in figure 5(*b*).

A more quantitative representation of the self-similarity of the front position is given by plots of the non-dimensional velocity, ξ_f, defined by (2.11), as shown in figure 6. With suitable choice of the virtual origin time (t_0), which accounts for the adjustment of the jet
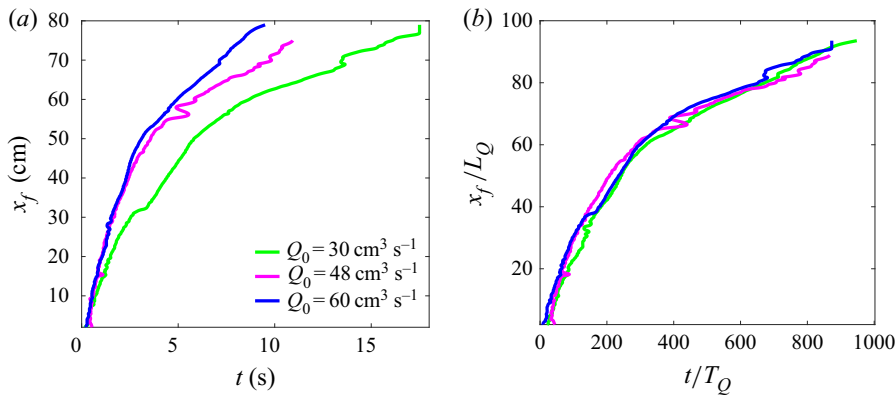
FIGURE 5. (*a*) Front position, x_f, versus time for three different Q_0 with $\phi_v = 0$ and $\beta = 8°$. (*b*) Scaling with jet length scale (L_Q) and time scale (T_Q).

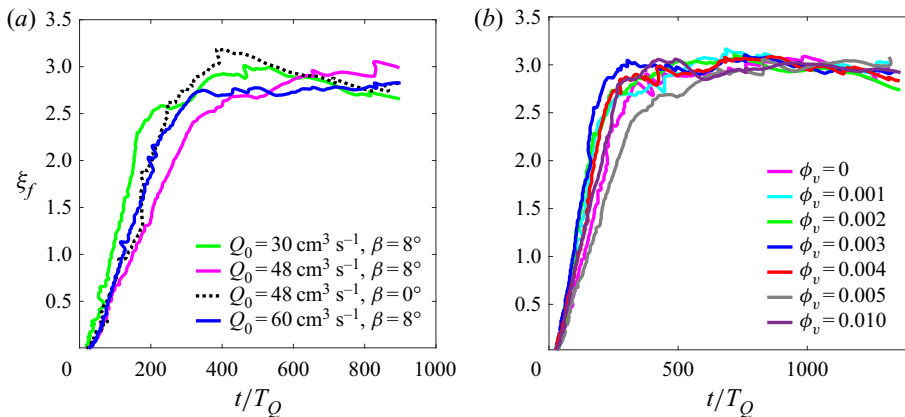FIGURE 6. (*a*) Non-dimensional velocity (ξ_f) defined by (2.11) corresponding to the scaled time (t/T_Q) for different Q_0 and β with $\phi_v = 0.005$ and $d_p = 120\,\mu m$. (*b*) Variation of ξ_f for different ϕ_v with $Q_0 = 48\,cm^3\,s^{-1}$, $d_p = 120\,\mu m$ and $\beta = 8°$.

front to self-similar form upon leaving the nozzle, the values of ξ_f are found to be constant after sufficient time. For $Q_0 = 48\,cm^3\,s^{-1}$, typical values of t_0 lie in the range 2–6 s. The corresponding non-dimensional front velocity ξ_f in our experiments was found to be $\xi_f \simeq 2.8 \pm 0.2$ which is moderately higher than the value $\xi_f \simeq 1.99 \pm 0.06$ measured for plumes (Bhamidipati & Woods 2017). As expected, ξ_f is not dependent upon the particle concentration ϕ_v, volume flux Q_0 or slope angle β.

Making use of the virtual time, t_0, to become self-similar, figure 7 plots the front position, scaled with L_Q, versus time with respect to the virtual time t_0, scaled by T_Q. For all experiments, these collapse to the semi-empirical prediction given by (2.11) at sufficiently large times.

By examination of the motion of injected red dye relative to the front, as shown in figure 2, we found the velocity scaling of the steady jet to be given by $\xi_0 \simeq 3.9 \pm 0.3$, so that $\xi_0 \simeq 1.4\xi_f$. Although the front position plotted in figure 7 shows that the initial adjustment to self-similarity extends a considerable distance from the source, the flow in the lee of the front is found to be self-similar, as confirmed by tracking the motion of
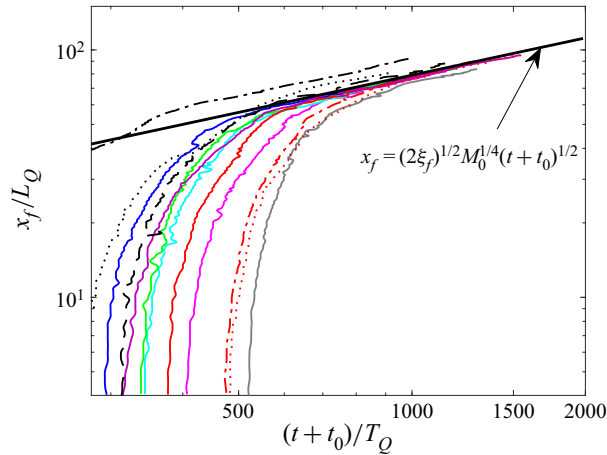
FIGURE 7. Scaled front position as a function of scaled time for various experiments with different ϕ_v, β, d_p and Q_0. All the solid curves correspond to varying ϕ_v and have the same parameters and colour scheme as that of figure 6(b). The black dotted and black dash-dotted lines correspond to $Q_0 = 30$ and $60 \text{ cm}^3 \text{ s}^{-1}$, respectively, with $\phi_v = 0$ and $\beta = 8°$. The red dotted and red dash-dotted lines correspond to $d_p = 88$ and $220 \text{ } \mu\text{m}$, respectively, with $\phi_v = 0.002$, $Q_0 = 48 \text{ cm}^3 \text{ s}^{-1}$, $\beta = 8°$. The black dashed line corresponds to $\beta = 0°$ with $Q_0 = 48 \text{ cm}^3 \text{ s}^{-1}$ and $\phi_v = 0$. The solid black line represents the theoretical scaling law for the front position.

injected red dye. Using (2.9), the measured value of ξ_0 corresponds to an entrainment parameter $\alpha_g \simeq 0.14 \pm 0.01$, which is more than twice the value typically measured for a free jet (Carazzo *et al.* 2006). This result is surprising given that the entrainment of a wall jet is expected to be smaller than the entrainment parameter, $\alpha_g \simeq 0.05$, for a free jet due to the existence of a no-slip condition near the wall and the suppression of meandering that, in comparison with the free jet, should reduce the length of the turbulent/non-turbulent interface between the jet and ambient fluid (Parker *et al.* 2020). This suggests that the finite depth of the ambient fluid may influence the entrainment process far from the source where the jet becomes self-similar, a consequence of the ambient fluid above the jet being directed back towards the source so that the total volume flux across a vertical-spanwise cross-section is always zero. Despite this discrepancy, it is anticipated that such a return flow has negligible influence upon sedimentation from the jet near the source, for which peak deposition occurs typically within $20 \text{ cm} \simeq 24L_Q$ from the source.

4.2. *Particle sedimentation*

From measurements of the height of the sediment taken at the end of an experiment (see, for example, figure 3), we extract the height of the sediment along the centreline of the jet, as shown in figure 8. In all cases, the height exhibits a large peak sometimes followed by smaller peaks in its lee. The largest peak typically has width of the order of 2 cm with steeper slope in the lee.

Generally, the distance, l_0, from the virtual origin to the peak sediment depth is larger if the source momentum flux is larger. This is consistent with the estimates for the length scales of deposition, L_p, L_s and L_c, respectively given by (2.13), (2.16) and (2.21). However, as shown in figure 9(a), when l_0 is scaled by L_p (the length scale that assumes deposition with no consequent bedload transport), the results show a strong dependence upon the
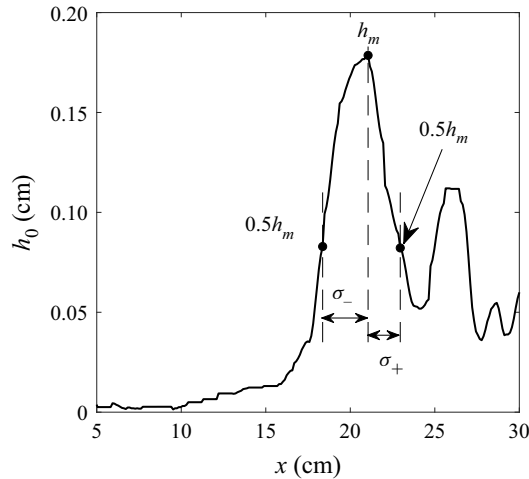
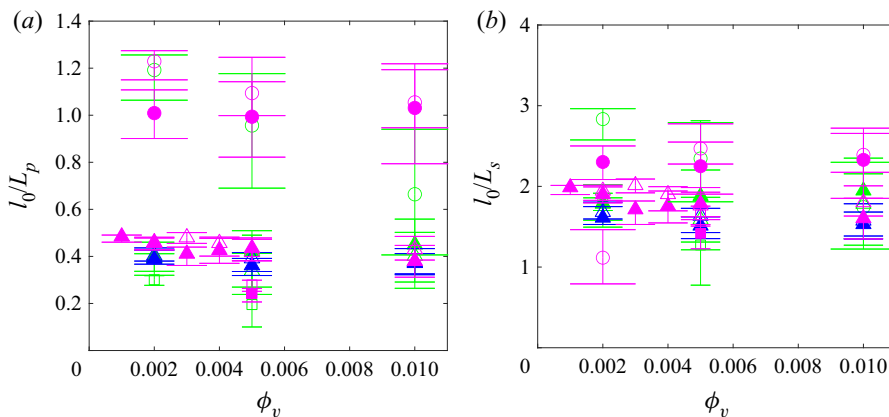FIGURE 8. Height distribution of the sediment along the jet centreline determined from Experiment 6.

FIGURE 9. Distance, l_0, from virtual origin of the maximum sediment depth measured from experiments for varying ϕ_v, d_p and β, given relative to scalings (*a*) L_p and (*b*) L_s. Colour represents Q_0 as indicated in figure 5. Filled symbols ($d_p = 88$ μm, squares; $d_p = 120$ μm, triangles; $d_p = 220$ μm, circles) for $\beta = 8°$. Open symbols ($d_p = 88$ μm, squares; $d_p = 120$ μm, triangles; $d_p = 220$ μm, circles) for $\beta = 0°$. Vertical bars indicate upstream half-width (σ_-) and downstream half-width (σ_+) as indicated in figure 8.

particle size. On the other hand, when l_0 is scaled by L_s (which includes the influence of bedload transport after settling but neglects the influence of the viscous boundary layer), all the data collapse reasonably well to relative values of $l_0/L_s \simeq 1.8 \pm 0.4$ (figure 9*b*).

A similar good collapse of data occurs in plots of $l_0/L_c \simeq 1.4 \pm 0.2$ (not shown). However, when the flow Reynolds number (2.17) is computed using $u = u_c(L_c)$, we find $Re_f \gg 1$. Hence the viscous boundary layer should not play a significant role in determining the critical Shields parameter.

We define l_s to be the along-jet distance from the virtual origin to where the sediment bed first appears. From measurements of l_s, we construct the ratio l_s/L_s, and so determine

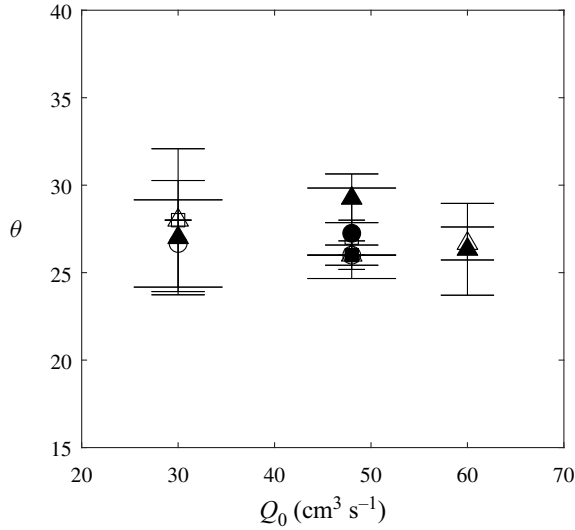FIGURE 10. Sediment deposit angles (θ, in degrees) for different Q_0. Symbols indicate the particle diameter, with $d_p = 88$ μm (■), 120 μm (▲) and 220 μm (●). Filled (open) symbols correspond to $\beta = 8°$ ($0°$). Bars represent the standard deviation computed for measurements over all ϕ_v values with fixed Q_0, d_p and β.

the value of the empirical constant γ_s appearing in (2.15) to be $\gamma_s = l_s/(\xi_0 L_s) \simeq 0.33 \pm 0.11$. The measured value of γ_s is used in (2.15) to predict the spanwise radius as a function of along-stream distance from the virtual origin where particles first sediment. In particular, this curve is superimposed on the plot of sediment depth in figure 3, showing good agreement to the location where sediment depth first becomes non-zero inside the teardrop-shaped deposit.

Near the source, the sediments deposit along lines at a near-constant angle from the source. The particles settle when the mean velocities at the periphery of the jet become sufficiently slow compared with the particle settling velocity. The measured angles of the sediment deposit determined from experiments with various Q_0, β and d_p are shown in figure 10. The angles are measured from the inside of the teardrop-shaped sediment bed. For each point, the error bars indicate the deviation for ϕ_v in the range of 0.1 % to 1 %. In all cases the angle ranges between $25°$ and $30°$.

In order to estimate the height scale determining the maximum sediment depth, h_m, we note that the volume of particles injected during the time t_f of an experiment is given by $V = Q_0 t_f \phi_v$. The particles are assumed to settle in a teardrop shape bounded inside by the curve given by (2.15) with $\gamma_s = 0.33$, and bounded outside by the same curve but with $\gamma_s = 1$, representing the condition that the kinetic energy of the flow is insufficient to overcome the potential energy of the particles. The basal area of this curve is given by

$$A = 2\sqrt{\frac{2}{\pi}} I \xi_0 (1 - \gamma_s^2) L_s^2, \tag{4.1}$$

in which $I = \int_0^1 x[\ln(1/x)]^{1/2} \, dx \simeq 0.313$. Thus, assuming a loose-sphere packing fraction of $p_f = 0.56$, and evaluating the constants in (4.1), the mean height is predicted to be

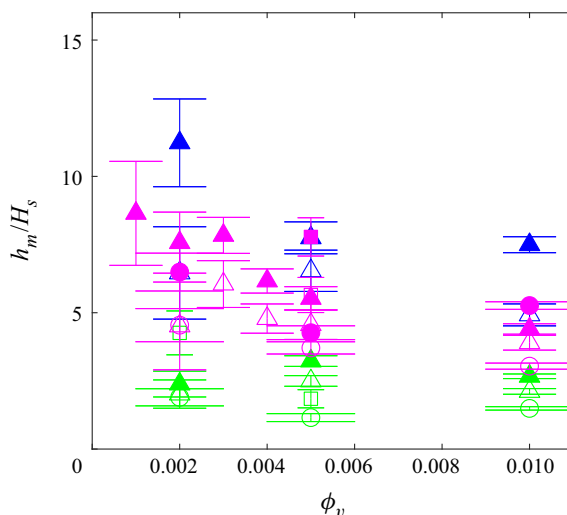$$H_s = \frac{1}{p_f} \frac{V}{A} \simeq (1.0 \pm 0.1) \frac{Q_0 t_f \phi_v}{L_s^2}. \tag{4.2}$$

FIGURE 11. Plot of measured maximum sediment depth normalized by the predicted mean depth for varying ϕ_v, d_p and β using scaling given by (4.2). Bars indicate the standard deviation among repeated experiments. Colour schemes and symbols are the same as those in figure 9.

As a test of the predicted height scale (4.2), figure 11 plots the measured values of the maximum height, h_m, normalized by H_s. As the maximum height is expected to exceed the mean, the figure shows that H_s correctly captures the order of magnitude of the expected mean sediment depth. However, there is clearly a trend such that the relative maximum depth is lower if the source volume (hence momentum) flux is smaller. For these experiments, the width of the sediment bed about the primary peak was found to be longer. This suggests that additional consideration should be made for the piling up of the sediment in front of the impinging jet and the influence of the bed morphology upon the jet itself near the lower boundary. Consideration of such dynamics lies beyond the scope of this study.

5. Conclusion

In this paper the spreading and sedimentation dynamics of horizontal and bottom-sloping dispersed particle-bearing jets in uniform ambient fluid were studied experimentally for a range of parameters, namely the particle volume fraction ϕ_v, source volume flux Q_0, particle diameter d_p and slope angle β. Our results show that irrespective of these parameters, the propagation of the jet front follows a self-similar behaviour. The relation between front position with time was found to be $x_f = (2\xi_f(t + t_0))^{1/2}M_0^{1/4}$ with $\xi_f \simeq 2.8 \pm 0.2$ and $t_0 = 4 \pm 2$ s. The flow in the steady jet behind the front advanced towards the front such that the non-dimensional velocity was $\xi_0 \simeq 1.4\xi_f$. The magnitudes of ξ_f and ξ_0 are larger than anticipated for an unbounded jet, suggesting that the finite depth of the ambient fluid influences entrainment and the jet speed far downstream of the source where the jet width is a non-negligible fraction of the total depth. Near the source where sediment deposition occurs the jet width is considered to be sufficiently small that finite-depth effects should not play a role in sedimentation.

Supposing that the radial profile of the jet assumes a Gaussian structure, a prediction was made for the momentum-settling length scale, L_p, at which the particle settling velocity

exceeds the mean turbulent flow speed. This provided a poor collapse of data. However, the prediction for the extent of the sediment bed improved on using the length scale L_s, which accounted for the bedload transport of particles after they settle out of the jet, neglecting viscous boundary layer dynamics. The observed teardrop-shaped structure of the sediment bed was well predicted using the bedload theory by choosing an empirical parameter $\gamma_s \simeq 0.33 \pm 0.11$ such that the maximum distance before settling begins was found to be $l_s = \gamma_s \xi_0 L_s$. On the other hand, the maximum height, when scaled by the corresponding mean height H_s, showed that the relative height was steeper and the peak more narrow if the jet momentum at the source was larger. Because the theory for the run-out length l_s already accounted for the decrease in the maximum jet velocity with distance from the source, it is believed that the dependence of h_m/H_s upon Q_0 and M_0 should also account for the influence of the growing sediment bed upon the jet itself. This will be the focus of future work.

Acknowledgements

Declaration of interests

The authors report no conflict of interest.

REFERENCES

BACIK, K. A., LOVETT, S., CAULFIELD, C. P. & VRIEND, N. M. 2020 Wake induced long range repulsion of aqueous dunes. *Phys. Rev. Lett.* **124**, 054501.

BALASUBRAMANIAN, S., MIRAJKAR, H. & BANERJEE, A. K. 2018 Role of dispersed particles on the dynamics of an umbrella cloud of a forced plume in a linearly stratified environment. *Environ. Fluid Mech.* **18**, 985–1006.

BHAMIDIPATI, N. & WOODS, ANDREW W. 2017 On the dynamics of starting plumes. *J. Fluid Mech.* **833**, 1–12.

BONNECAZE, R. T., HUPPERT, H. E. & LISTER, J. R. 1993 Particle-driven gravity currents. *J. Fluid Mech.* **250**, 339–369.

BONNECAZE, R. T. & LISTER, J. R. 1999 Particle-driven gravity currents down planar slopes. *J. Fluid Mech.* **390**, 75–91.

BROWN, P. P. & LAWLER, D. F. 2003 Sphere drag and settling velocity revisited. *J. Environ. Engng* **129** (3), 222–231.

CARAZZO, G., KAMINSKI, E. & TAIT, S. 2006 The route to self-similarity in turbulent jets and plumes. *J. Fluid Mech.* **547**, 137–148.

CHARRU, F., ANDREOTTI, B. & CLAUDIN, P. 2013 Sand ripples and dunes. *Annu. Rev. Fluid Mech.* **45**, 469–493.

EAMES, I. & DALZIEL, S. B. 2000 Dust resuspension by the flow around an impacting sphere. *J. Fluid Mech.* **403**, 305–328.

ERNST, G. J., SPARKS, R. J. S., CAREY, S. N. & BURSIK, M. I. 1996 Sedimentation from turbulent jets and plumes. *J. Geophys. Res.* **101**, 5575–5589.

FLECKHAUS, D., HISHIDA, K. & MAEDA, M. 1987 Effect of laden solid particles on the turbulent flow structure of a round free jet. *Exp. Fluids* **5**, 323–333.

GHARIB, M., RAMBOD, E. & SHARIFF, K. 1998 A universal time scale for vortex ring formation. *J. Fluid Mech.* **360**, 121–140.

GOMEZ, B. 1991 Bedload transport. *Earth-Sci. Rev.* **31**, 89–132.

HARDALUPAS, Y., TAYLOR, A. M. K. P., WHITELAW, J. H. & WEINBERG, F. J. 1989 Velocity and particle-flux characteristics of turbulent particle-laden jets. *Proc. R. Soc. Lond.* A **426** (1870), 31–78.

HERSEN, P., DOUADY, S. & ANDREOTTI, B. 2002 Relevant length scale of Barchan dunes. *Phys. Rev. Lett.* **89**, 264301.

HUNT, G. R. & KAYE, N. G. 2005 Lazy plumes. *J. Fluid Mech.* **533**, 329–338.

HUNT, G. R. & LINDEN, P. F. 2001 Steady-state flows in an enclosure ventilated by buoyancy forces assisted by wind. *J. Fluid Mech.* **426**, 355–386.

KNELLER, B. & BUCKEE, C. 2000 The structure and fluid mechanics of turbidity currents: a review of some recent studies and their geological implications. *Sedimentology* **47**, 62–94.

LEE, W. Y., LI, A. C. Y. & LEE, J. H. W. 2013 Structure of a horizontal sediment-laden momentum jet. *J. Hydraul. Engng ASCE* **139** (2), 124–140.

LIPPERT, M. C. & WOODS, A. W. 2020 Experiments on the sedimentation front in steady particle-driven gravity currents. *J. Fluid Mech.* **889**, A20.

MCCONNOCHIE, C. D., CENEDESE, C. & MCELWAINE, J. N. 2020 Surface expression of a wall fountain: application to subglacial discharge plumes. *J. Phys. Oceangr.* **50**, 1245–1263.

MEIBURG, E. & KNELLER, B. 2010 Turbidity currents and their deposits. *Annu. Rev. Fluid Mech.* **42**, 135–156.

MORTON, B. R. 1959 Forced plumes. *J. Fluid Mech.* **5**, 151–163.

MORTON, B. R., TAYLOR, G. & TURNER, J. S. 1956 Turbulent gravitational convection from maintained and instantaneous sources. *Proc. R. Soc. Lond.* A **234** (1196), 1–23.

MUNRO, R. J. & DALZIEL, S. B. 2005 Attenuation technique for measuring sediment displacement levels. *Exp. Fluids* **39** (3), 602–613.

PARKER, D. A., BURRIDGE, H. C., PARTRIDGE, J. L. & LINDEN, P. F. 2020 A comparison of entrainment in turbulent line plumes adjacent to and distant from a vertical wall. *J. Fluid Mech.* **882**, A4.

PICANO, F., SARDINA, G., GUALTIERI, P. & CASCIOLA, C. 2011 Particle-laden jets: particle distribution and back-reaction on the flow. *J. Phys.: Conf. Ser.* **318**, 052018.

DE ROOIJ, F. & DALZIEL, S. B. 2001 Time- and space-resolved measurements of deposition under turbidity currents. *Spec. Publs. Int. Ass. Sediment.* **31**, 207–215.

VAN REEUWIJK, M., SALIZZONI, P., HUNT, G. R. & CRASKE, J. 2016 Turbulent transport and entrainment in jets and plumes: a DNS study. *Phys. Rev. Fluids* **1**, 074301.

SHIELDS, A. 1936 Anwendung der Aehnlichkeitsmechanick und der Turbulenzforschung auf die Geschiebebewegung. PhD Thesis, TU Delft, the Netherlands.

SHUEN, J. S., SOLOMON, A. S. P., ZHANG, Q. F. & FAETH, G. M. 1985 Structure of particle-laden jets: measurements and predictions. *AIAA J.* **23**, 396–404.

SUTHERLAND, B. R. & HONG, Y. S. 2016 Sedimentation from particle-bearing plumes in a stratified ambient. *Phys. Rev. Fluids* **1**, 074302.

SUTHERLAND, B. R., ROSEVEAR, M. G. & CENEDESE, C. 2020 Laboratory experiments modelling the transport and deposition of sediments by glacial plumes rising under an ice shelf. *Phys. Rev. Fluids* **5**, 013802.